Causes and consequences of flow organization during melt transport: The reaction infiltration instability in compactible media

Marc Spiegelman

Lamont-Doherty Earth Observatory of Columbia University, Palisades, New York

Peter B. Kelemen

Woods Hole Oceanographic Institute, Woods Hole, Massachusetts

Einat Aharonov[1]

Lamont-Doherty Earth Observatory of Columbia University, Palisades, New York

Abstract. Geochemical and field evidence suggest that melt transport in some regions of the mantle is localized into mesoscale "channels" that have widths of 0.1–100 m or larger. Nevertheless, the mechanisms for formation of such channels from a grain-scale distribution of melt are poorly understood. The purpose of this paper is to investigate one possible mechanism for channel formation: the reaction infiltration instability (RII). We present numerical solutions of the full equations for reactive fluid flow in a viscously deformable, permeable medium. We show that dissolution in a compactible solid with a vertical solubility gradient can lead to significant flow localization such that $> 90\%$ of the melt flux is channelized in $< 20\%$ of the available area. In particular, the ability of the solid to compact enhances the instability by forming impermeable regions between channels. The combination of reaction, diffusion, and solid compaction leads to strong selection of preferred length scales with channel spacing smaller than the compaction length ($\delta \sim 10^2$–10^4 m). We explore the evolution of dissolution channels over parameter space and show that the behavior of the full nonlinear solutions is consistent with predictions from linear stability analysis. We also briefly consider the behavior of the instability in the presence of melting due to adiabatic decompression and demonstrate that significant localization can occur even in the presence of uniform melting and compaction. Using the linear analysis to extend these results for parameters expected in the Earth's mantle suggests that robust channel systems could form through the RII from a homogeneous system in ∼100,000 years with dominant channel spacing of 1–200 m.

1. Introduction

Understanding how melt flow is organized on scales ranging from the grain scale to the size of the partially molten region is a crucial problem in mantle and magma dynamics because the local distribution of melt affects the rates of melt transport, the composition of mantle melts, and the bulk rheology and dynamics of partially molten regions. There is geochemical and field evidence that although melting begins on the grain scale, melt transport must somewhere organize into "channels" that could range in scale from 10-cm spaced veins [*Spiegelman and Kenyon*, 1992] to episodic

[1]Now at the Weizmann Institute of Science, Rehovot, Israel, Environmental Sciences and Energy Research Department

dikes [*Sleep*, 1988; *Nicolas*, 1989, 1990] to multiscale "fractal trees" [*Hart*, 1993]. Nevertheless, the causes and consequences of channel formation remain virtually unexplored. The purpose of this paper is to investigate the physics, scaling, and observable consequences of one possible mechanism, the reaction infiltration instability (RII) [e.g., *Chadam et al.*, 1986; *Ortoleva et al.*, 1987; *Aharonov et al.*, 1995], where high-porosity channels form by a feedback between melt flow and corrosive dissolution. Previous authors have considered the behavior of this instability in rigid porous media and multicomponent water rock systems [e.g., *Steefel and Lasaga*, 1990, 1994; *Aharonov et al.*, 1997] and have demonstrated it experimentally [*Hoefner and Fogler*, 1988; *Daccord*, 1989; *Kelemen et al.*, 1995b]. Here we extend the problem to viscously deformable media, appropriate to the mantle, through a series of theoretical calculations for a simplified physical system.

The principal geochemical argument for flow localization in the mantle comes from the observation that mid-ocean ridge basalts (MORBs) are strongly out of chemical equilibrium with residual peridotites by the time they reach the crust-mantle transition zone. In terms of major elements, MORBs are not saturated in orthopyroxene (opx) at Moho pressures. However, opx is a major constituent of all residual mantle peridotites ($\sim 20\%$) [e.g., *O'Hara*, 1965; *Stolper*, 1980] and dissolves very rapidly in undersaturated mantle melts [*Kuo and Kirkpatrick*, 1985a, b; *Brearley et al.*, 1986; *Zhang et al.*, 1989]. Thus the observation that MORBs appear to have last equilibrated with mantle peridotite at a pressure of 1.0 GPa or more suggests that melts have traveled through at least the top 30 km of oceanic upper mantle without equilibrating with residual mantle peridotite. Similar arguments can be made from the observation that MORBs are also not in trace element equilibrium with most abyssal peridotites [*Johnson et al.*, 1990; *Johnson and Dick*, 1992]. They are usually interpreted to be a mixture of melts produced from mantle peridotite over a range of pressures that preserves information about pressures greater than that at the base of the crust [*Klein and Langmuir*, 1987; *Salters and Hart*, 1989].

These observations place important constraints on the melt transport process and are usually explained by a near-fractional melting process beginning at some depth, with only limited interaction between melt and residue during transport. While the depth at which disequilibrium transport begins is still an open question, *Spiegelman and Kenyon* [1992] showed that a minimum requirement for disequilibrium transport is for melts to be transported in veins or channels spaced $\gtrsim$10 cm apart assuming negligible interchannel porosity (or, e.g., $>$1 m apart for an interchannel porosity of 0.1%).

Beyond chemical arguments, there is also in situ field evidence for flow localization preserved in ophiolites which record melt migration features from both the adiabatically rising asthenosphere and the conductively cooled lithosphere [e.g., *Nicolas*, 1989, 1990; *Kelemen et al.*, 1995a; *Ceuleneer et al.*, 1996]. *Kelemen et al.* [1995a] provide a brief summary of these different features and identify a set of "replacive dunite" bodies in the Oman ophiolite as melt conduits [see also *Hirschmann*, 1995]. These dunites are regions where all of the orthopyroxene has been dissolved away, leaving a relatively unreactive olivine residue. The most important observation is that small, rare clinopyroxenes (cpx) in the dunites are chemically in equilibrium with MORB-like liquids, such as those that formed the igneous crust in the ophiolite, while similar pyroxenes in the adjacent harzburgites are not. These harzburgites are strongly depleted in light rare earth elements [*Kelemen et al.*, 1995a] and have pyroxene compositions similar to pyroxenes in abyssal peridotites [*Johnson et al.*, 1990; *Johnson and Dick*, 1992; *Dick and Natland*, 1996; *Ross and Elthon*, 1995].

The sharp geochemical contrast between residual harzburgites and replacive dunites suggests that the dunites are conduits for melt transport. Similar reactive dunites are seen in other ultramafic bodies and occur on scales from 0.1 to 100 m [e.g., *Quick*, 1981; *Kelemen et al.*, 1992; *Nicolas*, 1989; *Kelemen and Dick*, 1995]. Some of these dunites are associated with shear zones and dikes, but others have contact relationships which indicate that they formed as purely porous dissolution channels. While the dunites are clearly a locus for melt migration, questions remain as to how they form and how much melt has been channeled through them.

Previously suggested mechanisms for flow localization fall into two end-member categories. The first set of instabilities is purely mechanical, where local variations in matrix strength lead to flow localizations. These mechanisms include nucleation of "veins" into dikes or hydrofractures [*Nicolas*, 1989, 1990; *Sleep*, 1988; *Connolly and Podladchikov*, 1998] and the localization of melt by viscous shear of a material with porosity weakening viscosity [*Stevenson*, 1989; *Richardson*, 1998; *Hall and Parmentier*, 1998]. An alternative physicochemical mechanism, the reactive infiltration instability (RII) [*Chadam et al.*, 1986; *Ortoleva et al.*, 1987], has also been suggested as a means of melt extraction [*Kelemen et al.*, 1995b; *Aharonov et al.*, 1995, 1997]. In this mechanism, channeling arises from a feedback between dissolution and melt flux. In a system where the solubility of a mineral phase (e.g., pyroxene) in the melt increases with decreasing pressure in the melting column [e.g., *Kelemen et al.*, 1995b, Figure 3], regions of larger melt flux cause increased dissolution which increases the permeability, which in turn increases the flux in a runaway process.

Both mechanical and reactive instabilities are expected to occur in the mantle and should probably reinforce each other; however, because the dunite channels are clearly associated with dissolution features, in this study we begin by asking how much localization can be attributed to the reaction infiltration instability alone. The purpose of this paper is to investigate the simplest fully nonlinear problem appropriate for understanding the consequences of reactive flow in a compactible matrix. The discussion will consider additional process and compare our results to other studies.

2. Model Description

The simplest problem that demonstrates much of the physics of flow in reactive, deformable media is the flow of a solvent through a static (i.e. not upwelling) but compactible medium with a single soluble phase, in which the solubility of the phase increases with decreasing pressure (see Figure 1). This problem is discussed in detail by *Aharonov et al.* [1995] and is similar to that calculated for a rigid media by *Aharonov et al.* [1997]. This problem is also related to problem of flowing water through a box of salt and glass beads as modeled by *Kelemen et al.* [1995b].

2.1. Governing Equations

Appendix A provides a general derivation of the equations for reactive flow in viscously deformable porous media based on the original formulation of *McKenzie* [1984]. For the problem considered here, the equations can be written for four scalar variables: the porosity ϕ, the excess fluid pressure $\mathcal{P}$ (or compaction rate $\mathcal{C}$), and the concentration of the soluble phase in the solid c^s and the melt c^f. The dimensionless equations can be written

$$\frac{D_s\phi}{Dt} = (1-\phi_0\phi)\mathcal{C} + \Gamma, \tag{1}$$

$$-\boldsymbol{\nabla}\cdot k_\phi \boldsymbol{\nabla}\mathcal{P} + \frac{\mathcal{P}}{(\zeta+4\eta/3)} = -\boldsymbol{\nabla}\cdot[k_\phi(1-\phi_0\phi)\mathbf{k}] + \frac{\Delta\rho}{\rho_f}\Gamma, \tag{2}$$

$$\frac{D_s c^s}{Dt} = \frac{-\phi_0}{(1-\phi_0\phi)}(c^f_R - c^s)\Gamma, \tag{3}$$

$$\frac{D_f c^f}{Dt} = \frac{1}{Pe}\nabla^2 c^f + \frac{\rho_s}{\rho_f\phi}(c^f_R - c^f)\Gamma, \tag{4}$$

where ϕ is the volume fraction of melt present (ϕ_0 is a reference porosity), $\mathcal{C} = \boldsymbol{\nabla}\cdot\mathbf{V}$ is the "compaction rate" i.e. the rate of expansion or compaction of the solid phase [see *Spiegelman*, 1993a]. The compaction rate is related to the excess fluid pressure by

$$\mathcal{P} = (\zeta + 4\eta/3)\mathcal{C}, \tag{5}$$

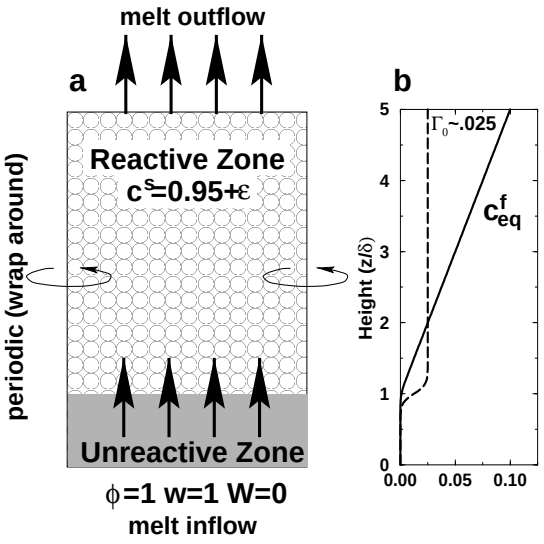

Figure 1. (a) Cartoon showing geometry of reactive flow model for a static but compactible matrix. In this problem the solution domain is 4×5 compaction lengths (129×161 grid points) where the upper 4δ are reactive with c^f_{eq} increasing linearly from 0 to 0.1. The lower boundary is near-constant flux inflow for melt with dimensionless $\phi = 1, w = 1$, upper boundary is free-flux outflow, and the sides are periodic (wrap around) boundaries. In this problem the solid velocity is $\mathbf{V} = 0$ to zeroth order. Initial conditions are $\phi = 1, c^f = c^f_{eq}$ and $c^s = 0.95 \pm \epsilon$, where ϵ is Gaussian white noise with variance of 10^{-4}. (b) Equilibrium solubility curve $c^f_{eq}(z)$ and the initial dissolution rate curve which for large values of Da approaches $\partial c^f_{eq}/\partial z = 0.025$ in the reactive zone.

where $(\zeta + 4\eta/3)$ is the viscosity that controls volume changes of the solid matrix. Additional notation is given in Table 1.

The full scaling of these equations is given in Appendix A, but for reference, all distances are scaled by the compaction length δ, which depends on the permeability and the ratio of solid and melt viscosities (see Equation (A14)). The compaction length governs the distance over which fluid pressure variations are transmitted through the solid phase [see *Spiegelman*, 1993a, b]. In rigid media, $\delta \to \infty$; however, estimates for the compaction length in the mantle are $\delta \sim 10^2$–10^4 m. In (1)–(5), time is scaled by the time it takes the melt to move one compaction length at the reference melt velocity w_0 (Equation (A15)). For the problems in section 2.2, however, it is often more convenient to scale by the time it takes melt to cross the entire system. For ref-

Table 1. Notation

Variable	Description	Value
Da	Damköhler number	10–160
Pe	Peclet number	10–160
ϕ_0	reference porosity	0.001–0.01
ϕ_c	compaction porosity	0.1–0.5ϕ_0
$c^f_{\max}$	maximum solubility in melt	0.1–0.3
h	system size	4–100δ
c^f_δ	solubility gradient	$c^f_{\max}/h$
n	permeability exponent	2
m	viscosity exponent	3
ϕ	porosity	
$\mathcal{P}$	excess pressure	
P	fluid pressure	
$\mathcal{C}$	Compaction rate ($\boldsymbol{\nabla}\cdot\mathbf{V}$)	
Γ	melting/dissolution rate	
$\mathbf{v}, \mathbf{V}$	melt/solid velocities	
c^f, c^s	melt/solid concentration	
$c^f_{eq}(P)$	equilibrium melt concentration	
δ	compaction length	10^2–10^4 m
w_0	percolation velocity	1–100 m yr^{-1}

erence, estimates of melt velocities in mantle systems range from 1 to 100 m yr^{-1} (or faster) and thus transit times for a 60-km-high melting region are ∼600–60,000 years.

Γ is the rate of mass transfer from solid to liquid which, for this problem, is the dissolution rate of the soluble phase. For tractability, and high resolution, we neglect multicomponent effects [see *Steefel and Lasaga*, 1994] and assume linear kinetics such that the dimensionless dissolution rate can be written

$$\Gamma = DaA'(c^f_{eq} - c^f), \tag{6}$$

where

$$Da = \frac{R\delta}{\rho_s\phi_0 w_0} \qquad A' = \frac{c^s(1-\phi_0\phi)}{c^s_0(1-\phi_0)}. \tag{7}$$

Da is the Damköhler number, which governs the amount of reaction that occurs in the time it takes the fluid to move one compaction length. R is the reaction rate constant (in kg m^{-3} s^{-1}), and w_0 is the melt velocity at porosity ϕ_0. A large Damköhler number implies rapid reaction relative to transport timescales, while a small Da implies little reaction. A' is the available surface area of the soluble phase (and goes to zero when the phase is exhausted); c^f is the concentration of the soluble phase in the liquid, and c^f_{eq} is the equilibrium solubility of that phase. For this problem the dissolution rate depends on the Damköhler number and the distance from equilibrium of the melt composition. For undersaturated melts, $c^f < c^f_{eq}$, $\Gamma > 0$, and the solid dissolves. $\Gamma < 0$ implies precipitation from a supersaturated melt. The permeability of the solid phase, $k_\phi = \phi^n$, is assumed to be a powerlaw in porosity; c^f_R is the concentration of the soluble phase entering the fluid due to the dissolution reaction (and here is just 1) and

$$Pe = \frac{\mathcal{D}^f\delta}{w_0} \tag{8}$$

is the Peclet number which controls the amount of diffusion or dispersion that occurs in the time it takes to advect one compaction length. A large Peclet number implies negligible diffusion.

Finally, the expressions D_s/Dt and D_f/Dt are the material derivatives for the solid and melt, respectively. For example,

$$\frac{D_f c^f}{Dt} = \frac{\partial c^f}{\partial t} + \mathbf{v}\cdot\boldsymbol{\nabla}c^f \tag{9}$$

is the time rate of change of melt concentration in a frame traveling at the melt velocity

$$\mathbf{v} = \mathbf{V} - \frac{k_\phi}{\phi}\left[\boldsymbol{\nabla}\mathcal{P} - (1-\phi_0\phi)\mathbf{k}\right]. \tag{10}$$

For small porosities, and no imposed solid flow field, the solid velocity in this problem is approximately zero. (Appendix A provides a more general derivation.)

Equation (1) governs the time rate of change of porosity which is controlled by the balance of physical compaction (or decompaction) and dissolution of the solid as measured in the frame of the solid. Equation (2) governs the excess fluid pressure (or compaction rate) due to variations in melt flux driven by gravity and the volume change on melting. This equation is discussed in detail by *Spiegelman* [1993a, c] and controls both compaction and the excess pressure gradients required to drive horizontal flow (e.g., Equation (10)). Equation (3) governs the change in concentration of the soluble phase in the solid. Equation (4) controls the change in melt concentration as measured in a frame moving with the melt.

Because these equations are dominated by advective terms and the balance between advection, diffusion, and reaction, they require highly accurate advection schemes. Here we have used a semi-implicit semi-Lagrangian algorithm [*Staniforth and Cote*, 1991] for the purely advective equations and a modified two-dimensional semi-Lagrangian Crank-Nicolson scheme for the combined advection-diffusion-reaction problem. Time stepping uses an iterative predictor-corrector method which converges rapidly. These schemes are unconditionally stable and have no Courant stability condition [see, e.g., *Press et al.*, 1992].

Thus time steps and spatial resolution are decoupled. Accuracy tests for the static runs suggest that time steps of 2–4 times the Courant condition are good values. At Courant numbers greater than 4 a standing wave artifact becomes noticeable in the static runs (although it does not change the overall physics) and we use a Courant number of 2 for the runs shown here. This artifact does not appear in the upwelling melting runs (Fig. 6) and for these we use a Courant number of 4. In two-dimensions, Crank-Nicolson style differencing results in large sparse sets of simultaneous linear equations as does the differencing of the elliptic equation (2). These equations are solved rapidly with multigrid methods, which scale linearly with the number of grid points. The combination of multigrid and semi-Lagrangian techniques allows efficient solution of these equations on very fine uniform grids in reasonable time.

2.2. Model Geometry and Details

Figure 1 shows the geometry and setup for the model we will investigate. For moderate resolution runs we use a box that is 4 compaction lengths wide by 5 high with a reactive zone that occupies the upper 4 compaction lengths of the box. The bottom compaction length of the box is an unreactive buffer to minimize the influence of the lower boundary. Figure 1b shows the initial equilibrium solubility c^f_{eq} as a function of height. In the reactive zone the dimensionless equilibrium solubility is a linear function of pressure given by

$$c^f_{eq} = c^f_\delta \left[(z-1) - \mathcal{P}\right]. \tag{11}$$

Thus solubility increases nearly linearly with height z, but excess fluid pressure causes a decrease in solubility at a given depth. The solubility gradient of pyroxene in the mantle is $\sim$1% kbar^{-1} [*Kelemen et al.*, 1995b, Figure 3] such that the maximum solubility over a melting column of height 60 km is $\sim$ 20%. We use a maximum solubility of 10% (i.e., $c^f_\delta = 0.025$ per compaction length) for the static runs and 20% for the melting runs. The initial solid concentration is $c^s_0 = 0.95 \pm \epsilon$, where ϵ is Gaussian white noise with variance of 1×10^{-4}.

Following a suggestion by *Sleep* [1988], this model also incorporates a porosity-dependent bulk viscosity for the solid matrix so that the dimensionless viscosity that controls compaction and fluid pressure is

$$(\zeta + 4\eta/3) = \frac{(\phi_c/\phi)^m + 4/3}{(\phi_c)^m + 4/3}, \tag{12}$$

which is nearly constant for porosities greater than the "compaction porosity" ϕ_c but becomes strongly incompressible at small porosities (i.e., $(\zeta + 4\eta/3) \to \infty$ as $\phi \to 0$). Other initial and boundary conditions are described in Figure 1a. General notation and adjustable parameters in this model are given in Table 1, although in practice we fix most of these parameters except the Peclet and Damköhler numbers.

3. Results

3.1. Basic Behavior

Figure 2 shows the evolution of porosity with time for a run with $Da = 40$ and $Pe = 40$ and shows the development of a series of high porosity channels that coalesce downstream (up section). By the end of this run ($t = 116$) the calculation has developed significant channels in porosity such that near the top of the box, 94% of the vertical flux is going through only 24% of the available area. Channels are defined as areas where the melt flux is greater than the mean flux at a given height. The maximum porosity in the channels is $\sim$3.9 times the original porosity. More significantly, strong localization arises because the porosity between the channels has been reduced to $\sim$0.1 of the original porosity due to compaction. Because the melt flux scales as ϕ^2, this implies that the maximum difference in flux between the channels and the interchannel region is a factor of $\sim$1500. The addition of compaction to reactive flow is a new feature in this problem and actually enhances the localization caused by this instability compared to rigid media [e.g., *Ortoleva et al.*, 1987; *Aharonov et al.*, 1997]. In particular, it leads to stronger localization and wavelength selection of channels with spacing smaller than the compaction length (see below).

We calculate the number of channels, the percentage of the total area occupied by channels, and the percentage of the total vertical flux at that height that is carried in the channels. A useful measure of the degree of flow localization is the "excess channel flux" F_c

$$F_c = \bar{F}\left(\frac{P_F}{P_A} - 1\right) \tag{13}$$

where $\bar{F}(z,t)$ is the mean vertical flux at height z, P_F is the percentage of flux in the channels, and P_A is the percentage of area covered by channels. For very weak oscillations of flux around the mean, $P_F \sim P_A \sim 50\%$, and therefore the excess channel flux is close to zero. When a large percentage of flux is carried in the channels and they occupy a very small area, F_c becomes large. Figures 3 and 4 show the evolution of the number of channels and excess channel flux for the numerical results illustrated in Figure 2.

Figure 3 shows the evolution in the number of channels and excess flux vertically averaged over the top region of the box from $z = 4.5$–5δ. At the top of the box the maximum number of channels (here about 3 per compaction length)

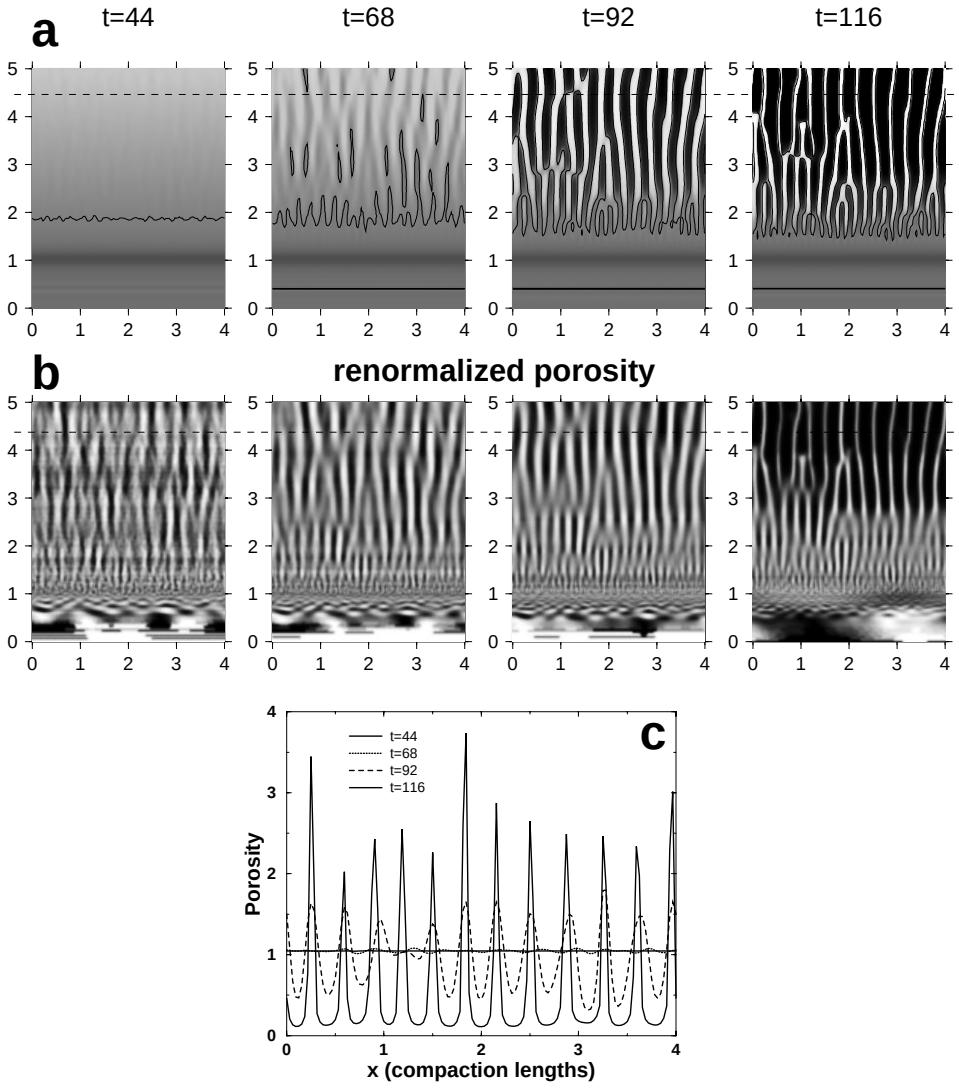

Figure 2. Evolution of porosity with time for a run with $Da = 40$ and $Pe = 40$. A dimensionless time of 1 in these runs is the time it takes to traverse the box once at the background porosity. At $t = 116$ the maximum porosity is 3.9% while the minimum porosity is only 0.1% due to compaction. In these runs the melt flux scales as ϕ^2 so that the flux is $\sim$1500 times greater in the channels than between them. (a) Absolute porosity with time. The contour is at $\phi = 1.01$. (b) Renormalized porosity with time. In each panel the porosity at each height z is renormalized such that $\phi_n = [\phi - \phi_{\min}(z)]/[\phi_{\max}(z) - \phi_{\min}(z)]$. (c) Cross section of porosity at $z = 4.5$ for the four panels in Figure 2a.

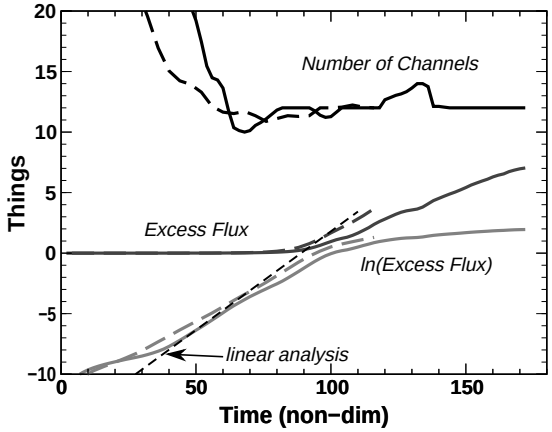

Figure 3. Evolution of mean number of channels and excess channel flux with time for the top 10% ($z = 4.5$–5) of the run shown in Figure 2. Dashed lines show values for a low-resolution run (129×161 grid points), and the solid line is for a high-resolution run (513×321 grid points) which runs longer. The total number of channels near the top of the box, quickly adjusts to around 12, while the excess channel flux is still negligible. However, for $t = 0$–90 the excess channel flux grows exponentially (the lower curve is $\ln(F_c)$) and then grows linearly with time from $t \sim 100$ when significant channeling begins.

is selected at approximately time $t = 50$, long before the excess channel flux significantly exceeds zero. Nevertheless, the excess flux is growing steadily and has two phases. In the earliest phase ($t \lesssim 100$) the excess channel flux grows exponentially with a doubling time τ of ∼5.3. This rate is comparable to, but slightly slower than, the growth rate of the fastest growing mode predicted by linear analysis ($\tau = 4.4$). The discrepancy may arise from the resistance to compaction caused by the porosity-dependent bulk viscosity (see Figure 6). Channels actually grow faster in runs that can compact more easily. When the channels begin to become significant ($F_c \gtrsim 1$), the excess flux grows nearly linearly from $t \sim 100$, with a slope of $dt/dF_c = 11$.

Figure 4 shows the number of channels and excess channel flux for the entire height of the box. At early times, the number of channels (∼30–40) is determined by the initial noise. The number of channels at the top of the box rapidly decreases to a nearly constant value of ∼10–12 and grows to a value of ∼50 channels at the bottom, thus producing a coalescing network. The overall number of channels is already determined by $t = 56$, although the excess flux is still negligible at this time. Figure 4b shows the evolution of the excess channel flux as a function of height and time and shows that it grows exponentially until $t \simeq 100$ and then grows linearly. Overall, the vertical structure of the channels in this run is quasi-steady state. Once formed, the channels tend to stay in the same place, although the tips and junctures may migrate (a movie of this and other runs can be found at http://www.ldeo.columbia.edu/∼mspieg/SolFlow/).

The change in number of channels with height can be predicted from the linear analysis (Equation (14)) by calculating the fastest-growing wavelength for a series of boxes of increasing height that have the same parameters per compaction length. This calculation is shown in Figure 4a and agrees well with the nonlinear solution. To demonstrate that this approximation is valid, Figure 5 compares the porosity fields for two runs with the same parameters per compaction length but with reaction zones of length 4δ and the 8δ. It is apparent that the number of channels predicted for a box of height 4 is a good approximation to the number of channels half way up a box of length 8.

The strong channeling is also apparent in other variables. Plate 1 shows the dissolution rate, solid concentration field, and melt concentration field for $t = 116$. Inspection of the dissolution rate field shows that significant dissolution occurs only in the channels. The solid concentration field shows the integrated dissolution for the entire run and shows strongly corroded regions corresponding to the channels. By design, these runs do not exhaust the soluble phase before the run ends. Thus they only approximate the initial stages in the formation of dunite channels in the mantle, in which orthopyroxene is completely dissolved. Finally, Plate 1 shows the variation in melt concentration and shows that it is slightly out of equilibrium in the channels. For lower Da the degree of disequilibrium is larger, while for larger Da it is smaller. Nevertheless, the instability will occur even under conditions of complete equilibrium transport, $Da \to \infty$ and, in fact, grows fastest for large Da.

3.2. Parameter Space

Plate 2 shows the behavior of this model in the parameter space spanned by Pe and Da. Plate 2 is effectively a phase diagram of 25 solutions in $\log Pe - \log Da$ space. The individual frames are shown at different times. However, times are the same for solutions with the same product of $DaPe$ (i.e., northwest-southeast trending diagonals). The choice of this time is driven by the linear analysis (section 3.3), which suggests that the product of $DaPe$ is the principal control on the behavior of these solutions. For any given value of Da, increasing the Peclet number increases the rate of channel growth and allows for more closely spaced channels because diminished diffusion allows more closely spaced chemical fluctuations to react before being diffused away. The spacing of the channels at the top of each box is nearly constant for a constant value of $DaPe$; however, higher values of the

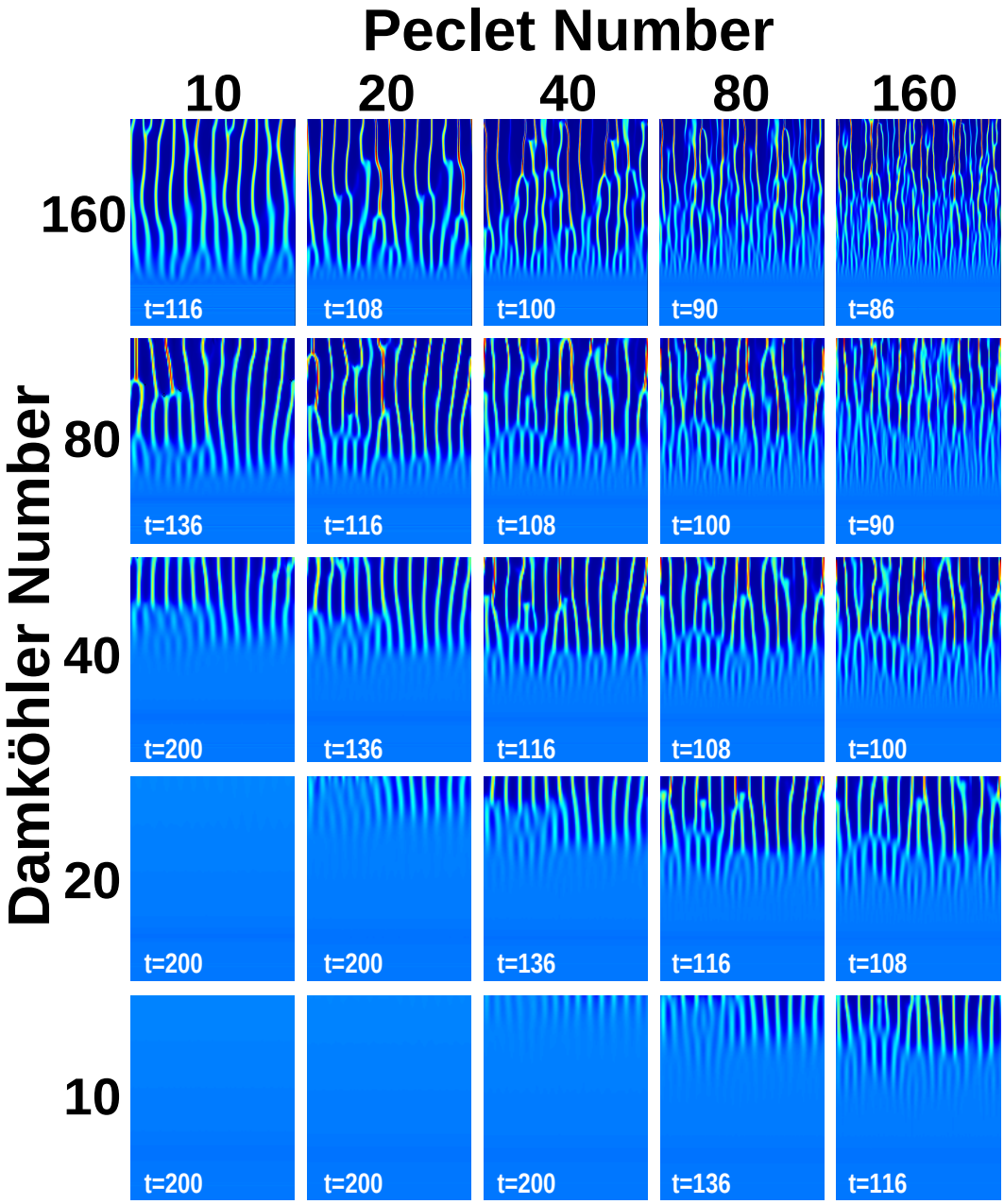

Plate 2. Behavior of the channeling calculation as a function of the two parameters the Dahmköhler number Da and the Peclet number Pe. Higher Da implies more rapid reaction. Higher Pe implies less diffusion. NW-SE diagonals show solutions for which the product of $DaPe$ is constant and are shown at equivalent times. The top five runs are actually higher-resolution runs (259×321 grid points) that are periodic in two horizontal compaction lengths.

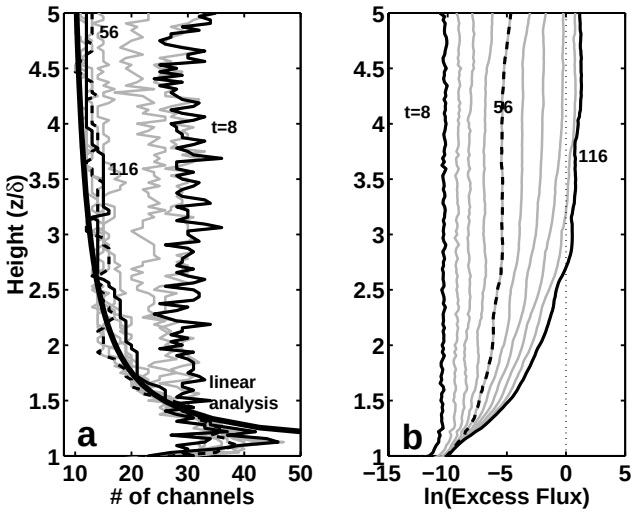

Figure 4. Evolution of channeling with height and time for run with $Da = 40$ and $Pe = 40$. Grey lines are vertical profiles at increments of $t = 12$. (a) Number of channels as a function of height and time. For this plot, a channel is a horizontally contiguous area at height z with a flux larger than the mean flux at that height. Heavy line shows the prediction of the number of channels with height from linear analysis. (b) Natural log of the excess channel flux F_c, as a function of height and time. F_c is the amount of excess flux above the mean that is carried in the channels. Note that the excess flux grows exponentially in time up to a time of about $t = 92$ and then begins to saturate. The vertical structure in the number of channels, however, is selected by about $t = 56$, long before any significant channeling occurs (i.e., $F_c \approx 1$).

Damköhler number allow for more robust channels over a larger portion of the reactive zone. For $Da = 160$, well-developed channels extend across the entire reactive zone. Preliminary results suggest that the size of the strongly channelized region depends on the ease of compaction at small porosities.

3.3. Comparison to Linear Analysis

Inspection of Plate 2 shows that there is a strong preferred wavelength of channeling in this problem and that the spacing and rate of growth of channels are principally functions of the product $DaPe$. A new linear analysis of this problem for large Da, based on the work of *Aharonov et al.* [1995], supports these claims and provides a useful framework for extending the numerical results to other problems. The principal result is a dispersion relationship for the exponential growth rate of porosity σ assuming porosity perturbations of the form $\phi^* \propto \exp[\sigma t + ikx + mz]$, where $k = 2\pi/\lambda$ is the horizontal wavenumber for horizontal features of wavelength λ and m (which is complex) controls the vertical structure. The dispersion relationship is slightly different from that given by *Aharonov et al.* [1995] and is given by

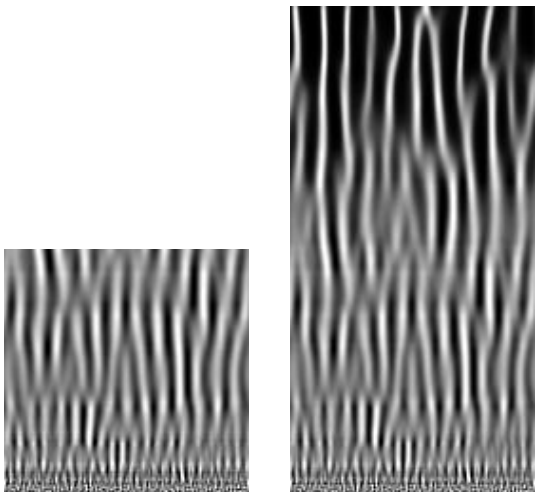

Figure 5. Normalized porosity at $t = 80$ for a short box with reactive zone of height 4δ and one with a reactive zone twice as long. The short box is almost identical to the lower half of the long run.

$$\sigma = \frac{n(m^2 - Bm)}{B(k^2 + 1 - m^2) + \Delta\rho/\rho_f} + \frac{nc_\delta^f[k^2 + 1 - m^2 + (m - B)(1 - 1/n)]}{B(k^2 + 1 - m^2) + \Delta\rho/\rho_f}, \quad (14)$$

where c_δ^f is the solubility per compaction length and $B = (k^2/DaPe + \rho_s/\rho_f)$ is the only parameter that depends on Da and then only as the product $DaPe$. Equation (14) scales σ to the time it takes melt to travel one compaction length. To scale to a "box-flushing" time, multiply by the height of the box in compaction lengths (here $h/\delta = 5$). The growth rate has two terms. The first is the growth rate due to viscous compaction, the second is the growth rate due to chemical dissolution. For the correct complex values of m chosen to match the boundary conditions, both terms (and therefore σ) are real.

The combination of these two terms is illustrated in Plate 3a which plots σ for the values of parameters used in the 25 runs shown in Plate 2. The compaction term is always negative but goes to zero for high horizontal wavenumbers because wavelengths much smaller than the compaction

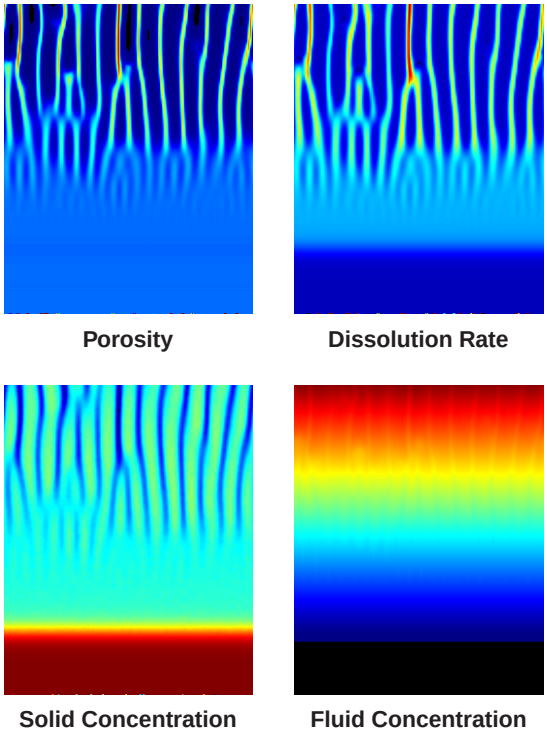

Plate 1. Porosity ϕ, dissolution rate Γ_R, solid concentration c^s and fluid concentration c^f calculated at time $t = 116$ for a run with $Da = 40$ and $Pe = 40$.

length are difficult to compact. The dissolution term is always positive and has a maximum value of $(\rho_f/\rho_s)nc_\delta^f$ for large Da and $k^2 < DaPe$. For horizontal wavenumbers $k > \sqrt{DaPe}$, diffusion becomes important and growth of very high wavenumber features is damped. The combination of compaction and diffusion gives rise to a strong peak in σ with significant wavelength selection. The preferred wavelength increases weakly with $DaPe$ while the growth rate increases considerably. Plate 3b shows the same plot as Plate 3a calculated from the numerical results of the 25 runs in Plate 2. Plate 3b shows a similar structure to Plate 3a, and is in good agreement with the linear analysis for large values of $DaPe$ (where the analysis is most appropriate) and large wavenumbers. Runs with $DaPe \lesssim 800$ have slower growth rates than predicted, which appears to be related to the viscosity effects and limitations of the analysis at lower Da. The discussion, however, suggests that values of $DaPe$ for the mantle are larger than the calculations shown here. Thus this analysis will be useful for estimating the behavior and efficiency of channeling for appropriate mantle parameters.

For example, for very large values of $DaPe$ expected in the mantle the maximum growth rate from the linear analysis is $\sigma_{\max} = (\rho_f/\rho_s)nc_\delta^f$ or rescaling to box-flushing times is

$$\sigma'_{\max} = \frac{\rho_f}{\rho_s} n c^{eq}_{\max}, \tag{15}$$

where $c^{eq}_{\max}$ is the maximum solubility at the top of the box. For the problems calculated here, $c^{eq}_{\max} = 0.1$ and $n = 2$, so $\sigma'_{\max} \sim 0.2$, which implies that at early times the most reactive problems will increase their porosity by a factor of e after five flushings of the box. In the mantle beneath ridges, n probably ranges between 2 and 4 and $c^{eq}_{\max} \sim 0.2$–0.3 for pyroxenes (see *Kelemen et al.* [1995b] for estimates of c^f_{eq} and *Aharonov et al.* [1995] for estimates of effective parameter ranges for the mantle). This range of parameters could reduce the growth time to around one to two flushing times.

The long times in these calculations before flow in the channels becomes significantly nonlinear stem from the very small initial perturbations that were used in our calculations in order to minimize the effects of the initial noise structure on the eventual wavelength selection. Figures 3 and 4, however, show that the instability is growing exponentially over the entire period. In a natural system with larger initial heterogeneity it is expected that saturation will occur much faster but that channel structure might lock onto any large initial permeability variations. The linear analysis also suggests that for extremely reactive systems with significant initial heterogeneity, channels may exist at a range of scales smaller than the compaction length. The discussion explores expected values for the overall parameters and suggests that efficient channel systems could form from this mechanism in order 100,000 years with channel spacings ∼1–200 m.

4. Discussion

The parameters in these numerical solutions were chosen to span a range that reveals most of the behavior of this solution while remaining numerically accessible in terms of resolution. Nevertheless, the question remains as to the appropriate values of δ, Da, and Pe for various Earth science problems of interest. The compaction length δ occurs in both the Damköhler number and the Peclet number and can be readily estimated for a very permeable one-dimensional adiabatic melting column as

$$\delta(z) \approx \left[\frac{(\zeta + 4\eta/3)W_0 F}{\Delta\rho g}\right]^{1/2}, \tag{16}$$

where W_0 is the solid upwelling velocity and $F(z)$ is the degree of melting as a function of height. This is the "reduced compaction length" of *Ribe* [1985] [see also *Spiegelman and Kenyon*, 1992]. Values of parameters appropriate for melting beneath mid-ocean ridges yield a range of compaction

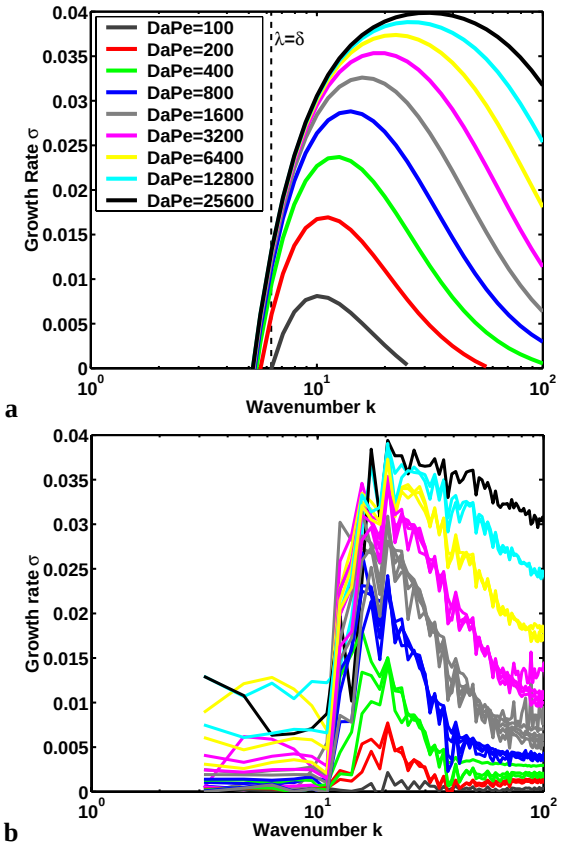

Plate 3. (a) Growth rates as a function of wavenumber as calculated from linear analysis using $c_\delta^f = 0.025$, and $n = 2$ which are the same as in the full numerical calculations. Choice of Da and Pe are also the same as in Plate 2. Note that the principal parameter controlling the growth rate is the product of Da and Pe; however, the wavelength that grows at the peak growth rate is not strongly sensitive to parameters. The Peclet number controls the amount of high wavenumber energy that is allowed to grow, but it is compaction (first term in equation (14)) that strongly damps the growth of long-wavelength modes with wavelengths much larger than the compaction length. (b) Average growth rate as a function of horizontal wavenumber measured for $z = 2.5$–4.5δ in Plate 2.

lengths from $\sim 10^2$ to 10^4 m. (For example, $W_0 \sim$ 1–10 cm yr^{-1}, $(\zeta + 4\eta/3) = 10^{18}$–$10^{21}$ Pa s, $\Delta\rho g \sim 5000$ Pa m^{-1} and $F \sim 0.1$–$0.2z/h$.)

Given a range of values for the compaction length, estimating the Damköhler and Peclet numbers reduces to determining how reactive and diffusive the mantle is on this length scale. In general, the Damköhler number can be rewritten as $Da = \delta/L_{eq}$, where L_{eq} is the "equilibration length," that is, the distance that a parcel of fluid will travel before equilibrating with the matrix. A short equilibration length relative to the compaction length implies a high Da. *Aharonov et al.* [1995] (Appendix A) discuss estimates for L_{eq} in some detail and give values from 10^{-7} to 100 m. The lower values assume reaction rate constants appropriate for the dissolution of pyroxenes in a well-mixed, undersaturated melt [e.g., *Kuo and Kirkpatrick*, 1985a; *Brearley et al.*, 1986] and slow melt migration, whereas the higher values are based on assumptions of more limited interaction between melts and pyroxene [*Zhang et al.*, 1989] and faster melt migration. Either way, the equilibration length is still significantly smaller than the compaction length, which implies that in the mantle, if undersaturated melts have ready access to soluble minerals, then dissolution reactions can occur extremely rapidly.

A similar argument for the Peclet number suggests that diffusion is likely to be negligible, and therefore Pe should also be large. The Peclet number can be rewritten as $Pe = \delta/L_{\rm diff}$, where $L_{\rm diff}$ is the length scale over which diffusive/dispersive effects are important. If diffusion is controlled by molecular diffusion within the melt phase, $L_{\rm diff}$ is likely to be very small because liquid diffusivities are of order 10^{-12} m^2 s^{-1}. For melt velocities 1–1000 times solid upwelling velocities the diffusion length due to molecular diffusion alone would still be $L_{\rm diff} \ll 1$ m with Peclet numbers $> 10^6$. In a permeable flow system, however, it is likely that horizontal smearing of chemical fluctuations will be caused by hydrodynamic dispersion as well as chemical diffusion. For a dispersivity of $\alpha =$ 1–10 m the effective diffusivity would be $\mathcal{D}^f_{\rm eff} = \alpha w_0$, and the Peclet number would be $Pe \sim \delta/\alpha$. Even at quite high melt velocities, these dispersivities give estimates of $Pe \sim$ 10–10,000. The lower of these values would imply some diffusion. However, an upper bound on the diffusion length can probably be placed by the observation that dunite channels and reaction zones around pyroxenite dikes in the mantle section of ophiolites preserve mineral compositions that are distinct from those in surrounding, residual peridotites [e.g., *Quick*, 1981; *Kelemen et al.*, 1992, 1995a; *Takahashi*, 1992; *Varfalvy et al.*, 1996]. Moreover, if channels can begin to form by compaction localization, the very low permeabilities between channels should limit the dispersivity and interchannel diffusion.

All of these arguments taken together suggest that the values of Da and Pe appropriate for melting beneath mid-ocean ridges are significantly larger than the most reactive and least diffusive run shown in Plate 2. If so, then the channeling instability is likely in the upper mantle and will grow at a rate close to the maximum growth rate (Equation

(15)) for wavelengths smaller than the compaction length and larger than $\sim 2\pi\delta/\sqrt{DaPe}$. Using the linear analysis as a guide, we can estimate the growth rate and channel spacing for a range of mantle conditions. As an example, consider a melting column 75 km high with a maximum solubility of 0.25, permeability exponent 2, compaction length $\delta = 1$ km, $Da = Pe = 1000$, and melt velocity $w_0 \sim 10$ m yr^{-1}. The e-folding time for the instability is about two flushing times (here $t_{\rm flush} = 7500$ years) so we might expect significant channeling to form from a homogeneous system, at this growth rate, in 100,000–150,000 years (see section 4.1). At this large value of $DaPe$ the preferred channel spacing is $\sim$17 channels per compaction length (60 m) but all wavelengths between 20 and 160 m grow at rates greater than $>$95% of the maximum growth rate.

4.1. Adding Melting as Well as Reaction

The previous analysis has been based on simple scaling arguments for 1-D steady state melting columns. However, the problem we have been considering thus far does not actually include melting. In decompression melting regimes such as the region beneath mid-ocean ridges, "background melting" adds porosity to regions that would otherwise compact to near impermeability in systems where additional melt is produced only by reaction (e.g., Plate 2). In addition, the rising solid will have only a finite residence time in the melting region.

In the calculations shown so far, we have assumed that the solid is stationary relative to the melt and can be fluxed indefinitely with a solvent. In an adiabatic melting system the time-integrated flux of solvent through a piece of solid depends on the size of the system and the relative velocities of melt and solid. If we scale to the time it takes melt to cross the system, then for a low-permeability system in which the velocities of melt and solid are the same, the solid will cross the system in a time of 1. In this case, the solid will only see the melt that was produced locally, and channeling will not occur. For a higher permeability system, however, the solid will move more slowly than the melt. In this case, a significant flux of melt will pass through the rock, and channeling will occur. Thus the numerical results presented in section 3 can be viewed as solutions to the limiting case of an infinitely permeable system. The question remains what happens when melting is included and the permeability is finite.

Appendix A provides the additional equations required for a background melting rate proportional to the solid upwelling rate W_0. Figure 6b shows results for porosity for a melting run with $Da = 80$ and $Pe = 160$ and a mean melt velocity $\sim$200 times the solid upwelling velocity. Strong, compaction driven channels are produced with spacings comparable to the static run with the same Da and Pe (Plate 2). Unlike the static runs, however, this problem evolves to a quasi-steady state where the maximum channel porosity at any height is roughly constant with time. For Figure 6b the maximum porosity is $\sim 5\phi_0$ and the minimum porosity is $\sim 0.3\phi_0$. Significant channels are seen at ~ 15 flushing times and the steady state is achieved by 25 flushing times. For this problem, the channels only occupy the upper two compaction lengths of the box.

Additional runs (Figures 6a and 6c), however, suggest that both the growth rate and the size of the region with significant channels in the melting runs depend on how compactible the medium is. For the melting runs in Figure 6 the matrix becomes harder to compact for porosities much less than the compaction porosity ϕ_c (see Equation (12)). Figure 6a shows the same problem as Figure 6b but is easier to compact and produces significant channels over a larger region in less time than Figure 6b. Figure 6c is more difficult to compact than Figure 6b and channels grow slowly and are only significant in the upper compaction length. A run with $\phi_c = 0.5\phi_0$ (not shown) has negligible channels. More work needs to be done to quantify this phenomenon. However, it emphasizes an important feature of this paper, that compaction strongly enhances flow localization by producing low-permeability interchannel regions.

4.2. Observational Constraints on Channeling

Give the behavior of the simplest reactive channeling problems, here we review and amplify the important observational constraints that can be compared and contrasted with theory.

4.2.1. Chemical disequilibrium. We emphasize the central observation that primitive mid-ocean ridge basalts are observed to be in neither major nor trace element equilibrium with shallow, residual mantle peridotites [e.g., *O'Hara*, 1965; *Stolper*, 1980; *Johnson et al.*, 1990; *Johnson and Dick*, 1992]. Both orthopyroxene undersaturation and trace element disequilibrium imply that primitive mid-ocean ridge basalts must have last equilibrated with mantle peridotite at a pressure of 1.0 GPa or more. Such liquids must pass through the top 30 km, or more, of the oceanic upper mantle without equilibrating with residual mantle peridotite. This constraint can be satisfied by very rapid transport (e.g., in melt-filled fractures) so that the diffusion time is short, or by slower porous flow in wide dunite conduits, so that the distance between migrating melt and residual peridotite is longer than the diffusion distance.

4.2.2. Melt migration features in mantle samples. The characteristics of melt migration features in the mantle section of ophiolites and in drill core from the oceanic mantle were reviewed by *Kelemen et al.* [1997]. They may

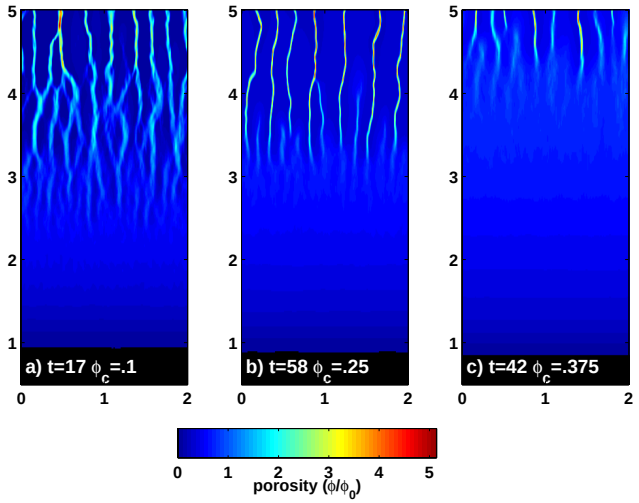

Figure 6. Comparison of porosity for three melting runs with $Da = 80$ and $Pe = 160$ and three different values of the compaction porosity ϕ_c. The degree of melting F increases linearly from 0 at the base of the reactive zone ($z = 1\delta$) to 20% at the top ($z = 5\delta$), while the solubility of the soluble phase increases linearly from 0.2 to 0.4 across the reaction/melting zone (thus $c^f_\delta = 0.05$ is twice as large as in Plate 2). The scale porosity is $\phi_0 = 0.001$, and thus the scale melt velocity is roughly 200 times faster than the solid velocity. (a) Easily compactible run $\phi_c = 0.1\phi_0$ which develops a robust channel system over more than half of the column in ~ 10 flushing times. The run stopped at $t = 17$ due to extreme permeability variations ($\phi_{\min} = 0.09\phi_0$). (b) Moderately compactible run which goes to a quasi-steady state channel system by $t = 25$ ($\phi_{\min} = 0.3\phi_0$). (c) Poorly compactible system which produces a weaker steady channel network after $t \sim 30$ ($\phi_{\min} = 0.45\phi_0$).

be classified into two groups: dikes and dunites. Dikes are composed of igneous pyroxenes and plagioclase, as well as minor olivine, which crystallized from melt migrating in an open fracture. Their compositions require conductive cooling of migrating melt, and they are typically undeformed, indicating that they have not undergone corner flow beneath a spreading ridge. Thus it is inferred that they formed off-axis in a conductive boundary layer. Dunites commonly show evidence for extensive ductile deformation along with their host peridotites and could form from migrating melt in the adiabatically upwelling region beneath a ridge. Many dunites also show contact relationships that indicate that they form by replacement, as a result of dissolution of pyroxene from mantle peridotite in melt migrating by porous flow. Rarely if ever are mantle dunites formed by crystallization of olivine in a melt-filled, open fracture.

Thus observed melt migration features in ophiolite mantle and drill core from oceanic mantle indicate that dunites, formed as a result of reactive flow of melt, are important conduits for melt extraction. There is no field evidence which requires melt migration in fractures in the adiabatically upwelling region of the mantle, except in the shallowest mantle. Furthermore, *Kelemen et al.* [1997] showed that focused flow of melt in porous conduits could satisfy melt velocity constraints derived from uranium series disequilibria in lavas (e.g., data compilations of *Sims et al.* [1995] and *Lundstrom et al.* [1995]) and from the timing of volcanism due to decompression melting following deglaciation in Iceland [*Jull and McKenzie*, 1996; *Slater et al.*, 1998].

These observations are consistent with an important role for the reactive infiltration instability (RII) in mantle melt extraction. However, it does not follow that the geological evidence requires extensive channels formed by the RII. Migration of melt in fractures within the melting region cannot be ruled out on the basis of geological or geochemical evidence. Adiabatic ascent of melt within a fracture in the melting regime would produce no crystallization, so no dike would form. Reaction zones along the walls of such fractures would be composed of replacive dunite.

Thus it is possible that some or all dunites form as porous reaction zones around melt-filled fractures, as proposed by *Quick* [1981], *Nicolas* [1989], and *Suhr* [1999]. Perhaps such a mechanism, near the transition from the adiabatic region to the conductive thermal boundary layer, forms small dunites, <1 m wide, which contain medial pyroxenite or gabbro dikes, such as are locally observed in the Trinity, Josephine, and Oman ophiolite mantle sections and in drill core from the shallow mantle from the East Pacific Rise [e.g., *Quick*, 1981; *Boudier and Coleman*, 1981; *Kelemen and Dick*, 1995; *Dick and Natland*, 1996]. It is less likely that large dunites, up to 100 m wide in the Oman mantle section, form as reaction zones around a single crack.

Clearly, it is possible to envision melt migration mechanisms intermediate between open, melt-filled fractures and porous conduits and combinations of mechanical and chemical instabilities that can form dunites. The RII with compaction leads to significant flow localization by itself, which is probably enhanced by mechanical instabilities, and both types of instabilities are likely to occur together in the mantle. Significant work remains, however, to understand these more complex instabilities and their diagnostic observable features.

4.2.3. Focusing of mantle melt extraction to the ridge axis. Despite the fact that fracture-controlled melt migration mechanisms in the melting region cannot be ruled out

on the basis of outcrop-scale geologic evidence, plate-scale observational constraints can be used to argue that relatively simple porous flow within a viscously compacting solid matrix is probably the dominant mechanism of melt transport in the melting region beneath oceanic spreading ridges. The combination of two crucial observations, (1) that the igneous ocean crust at fast spreading ridges reaches 95% of its total thickness within 2 km of the ridge axis [e.g., *Vera et al.*, 1990] and (2) that modeling and seismic data suggest that the region of partial melting is of the order of 100 km wide at its base [e.g., *Barnouin-Jha et al.*, 1997; *Forsyth et al.*, 1998], requires that melt transport occurs via mechanisms which focus melt flow toward the ridge axis. As noted by *Sleep* [1988], melt extraction in fractures spanning the melting region in mantle undergoing passive, corner flow beneath a spreading ridge cannot satisfy this constraint because such fractures, formed parallel to the direction of maximum compressive stress, would reach the top of the mantle over a region more than 80 km wide.

If solid mantle upwelling is focused into a narrow column directly beneath the ridge, then perhaps melt flow in fractures could produce focused accretion of igneous crust within 2 km of the ridge axis. However, seismic results from the Mantle Electromagnetic and Tomography (MELT) experiment do not require focused solid upwelling [*Forsyth et al.*, 1998], and may rule out focused upwelling geometries. Also, some extremely focused solid upwelling geometries, such as those required to focus all melt extraction to a narrow region beneath ridges, produce melts with compositions unlike MORB [*Spiegelman*, 1996]. Thus it seems that melt migration primarily controlled by fractures cannot produce the observed coalescence of melt extraction toward spreading ridges.

In contrast, a variety of porous flow mechanisms have been proposed to explain coalescence of melt toward ridges: (1) "suction" due to corner flow [*Spiegelman and McKenzie*, 1987; *Phipps Morgan*, 1987]; (2) anisotropic permeability along mineral foliation [*Phipps Morgan*, 1987] or in stress controlled planes of high porosity [*Daines and Kohlstedt*, 1997; *Zimmerman et al.*, 1999]; (3) channels at the base of the "lithosphere," beneath a permeability barrier created by melt crystallization [*Sparks and Parmentier*, 1991; *Spiegelman*, 1993c]; and coalescence of dissolution channels, as illustrated in Figures 2–5 and Plates 1 and 2.

Individually, each of these may be insufficient to explain melt focusing to the ridge. Mechanism 1 requires mantle viscosities higher than estimated, particularly in high temperature mantle such as beneath Iceland [review in *Hirth and Kohlstedt*, 1996]; mechanism 2 requires foliated peridotites and/or non-hydrostatic stress, which may not be present in much of the melting region; mechanism 3 should form "impregnated peridotite," residual mantle combined with interstitial products of melt crystallization, above dunite in ophiolites, but this is not observed; and ongoing modeling of mechanism 4, presented in this paper, suggests that the aspect ratio of coalescence is insufficient to focus melt from, e.g., a 100-km-tall melting region, 100 km wide at the base, into a 5-km-wide zone beneath the ridge.

However, combinations of these 4 mechanisms may be sufficient to explain focused melt extraction beneath ridges. Unstable formation of dissolution channels by decompressing melt is enhanced by melt flux and intrinsically follows pressure gradients in the liquid. High melt flux and lateral pressure drops toward the ridge axis due to mechanisms 1 and 2 will lead to the formation of the largest channels beneath the ridge, and of diagonal dissolution channels converging toward the ridge. Also, a variant of mechanism 3 is likely, particularly beneath slow spreading ridges. Diagonal isotherms near the top of the melting region may drive formation of diagonal dissolution channels converging toward the ridge.

Thus coalescence of melt transport from a broad melting region to a narrow region of igneous crustal accretion beneath oceanic spreading ridges seems to require that the dominant mode of melt transport is via a combination of porous melt migration mechanisms. If melt migration is dominantly by porous flow then this, in turn, requires that melt migration through the upper 30 km of the mantle beneath ridges occurs in wide, porous dunites conduits, which shield migrating melt from equilibrating with residual mantle peridotite. Thus the RII may well be an important factor in controlling melt migration in the upper mantle beneath ridges.

4.3. Comparison of Model Results and Observations

Because the numerical model considered in this paper is greatly simplified compared to the actual process of melt extraction from the mantle beneath oceanic spreading ridges, it may be premature to directly compare modeling results to field observations. However, here we try to look toward the future, to anticipate how the application of the theory of RII to mantle melt extraction may be tested and refined.

There are two intrinsically different types of models presented in this paper, those with solvent migrating through a static solid matrix (Figures 1–5 and Plates 1–3), and those which incorporate an upwelling solid matrix and decompression melting (Figure 6). Each is potentially comparable to different mantle samples. Results of modeling with a static solid matrix may have relevance for environments on Earth in which melt rises into nearly static, overlying mantle peridotite; for example, migration of melt in the shallow mantle beneath subduction-related magmatic arcs might be approx-

imated in this way provided that solubility of pyroxene increases upward in such settings. In many ophiolites, such as the Trinity, Josephine, and Ingalls ophiolites near the U.S. West Coast, late- and post-kinematic replacive dunites preserve evidence for melt migration through nearly static mantle [*Quick*, 1981; *Kelemen et al.*, 1992; *Kelemen and Dick*, 1995, and our unpublished data]. For mid-ocean ridges and for the early features of the Oman ophiolite, formed beneath an active oceanic spreading ridge, the results of modeling including decompression of the solid matrix are more relevant.

Of course, many aspects of the simple models presented in this paper do not adequately simulate dunite formation in the mantle. As noted, none of the models shown here reach exhaustion of the soluble phase (but see www.ldeo.columbia.edu/∼mspieg/SolFlow), whereas it is common to find mantle dunites which are completely free of pyroxene. Furthermore, division of the solid matrix in the models into "soluble" and "insoluble" components is not strictly correct, since even the refractory minerals olivine and spinel, which compose dunites, are slightly soluble in adiabatically ascending mantle melts. We have also neglected more complex multicomponent reactions as considered by *Steefel and Lasaga* [1994]. These will be investigated in future studies.

Another crucial divergence between dissolution channels in simple models and observed mantle dunites is their three-dimensional morphology. Although the numerical results presented in this paper are two-dimensional, *Aharonov et al.* [1997] presented three-dimensional results of numerical models of the RII in rigid, soluble porous media. In those results, dissolution channels were roughly cylindrical, whereas most dunites in the mantle section of ophiolites are tabular features. Nevertheless, these 3-D models did not include compaction, which clearly enhances the instability in two dimensions. As it is easier to compact tabular features than cylindrical ones, it may be that compaction in three dimensions leads to tabular features; however, this remains to be tested with further modeling. Alternatively, it may be that natural, tabular dunites result from preexisting foliation in mantle peridotites, for example, anisotropic permeability due to crystal shape and/or lattice preferred orientation, or the presence of tabular pyroxene-rich banding [*Dick and Sinton*, 1979].

Comparison of quantitative model results to field observations is rendered difficult by the fact that the instantaneous and time-integrated values of most calculated parameters, e.g., melt flux, continue to vary throughout the model runs, whereas mantle outcrops preserve only the final, time-integrated effects of melt migration. An exception to this is the quasi-steady state structure of the coalescing channel networks illustrated in Figures 3, 4, and 6a. Because this structure remains nearly constant in time and space in the model results, it has the potential for direct comparison to similar structures formed in the mantle. Currently, this is not straightforward, because the models do not reach phase exhaustion, so the final width of "dunite" channels has not been determined in the numerical results. Conversely, the width of dunite channels in the field is easily measured, but the time-integrated flux of melt through the dunites is much less well-constrained.

We can make a start at comparing numerical results and field observations by assuming that the final width of dunite channels is related to the flux of melt through the channels. In Figure 7, we show flux/frequency and size/frequency statistics for channel networks from models and from mantle outcrops in the Ingalls ophiolite [*Kelemen et al.*, 2000]. Figure 7a illustrates the power law relationship for flux/channel versus number of channels with a given flux defined by an idealized, coalescing network in which flux is preserved downstream ("Einat's Castle" [*Aharonov et al.*, 1995, Figure A1]). Figure 7b shows the same relationship in results of the numerical model illustrated in Figures 2–5 and Plate 1. The slopes in Figures 7a and 7b are the same because nearly all the melt in the numerical model migrates in channels and flux is conserved downstream through the coalescing network. Figure 7c is a plot of channel width (intercept length) versus number of channels with a given width (per meter of intercept measurements) in three outcrops from the Ingalls ophiolite in the Washington Cascades, which also shows a power law relationship albeit with a different slope. To make the current data on size/frequency relationships for dunites consistent with the flux/frequency relationships in our numerical modeling results requires that the flux in the dunites is proportional to the dunite width. However, it is possible that other melt migration mechanisms could give rise to a power law relationship between dunite size and frequency, so that the qualitative similarity between observations and our model results cannot be taken as a confirmation that the RII is responsible for forming dunites in the Ingalls ophiolite.

More complete tests of the applicability of the RII to melt extraction from the mantle beneath oceanic spreading ridges await completion of more elaborate numerical models and further characterization of the spatial relationships and integrated melt flux for dunites in mantle outcrops. Also, it will be important to develop quantitative, predictive models for other melt migration mechanisms, such as hydrofracture, to search for spatial relationships which might be diagnostic of a particular transport mechanism. Nevertheless, these initial results suggest that strong flow localization can form from coupled fluid-solid process associated with melt transport.

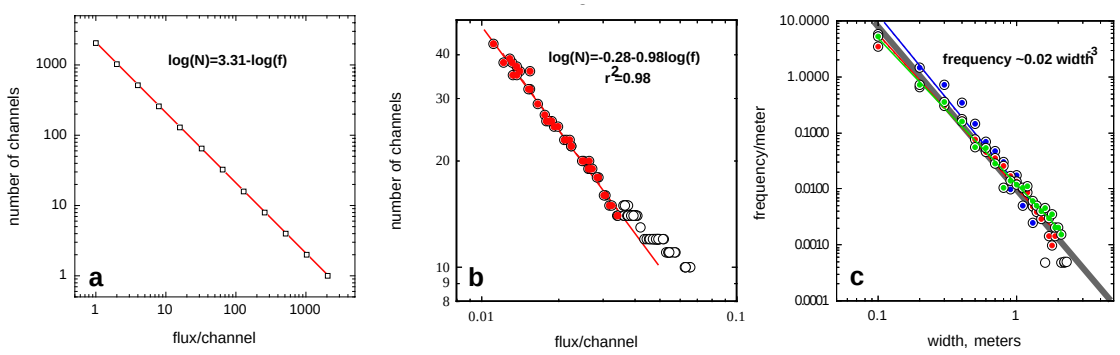

Figure 7. Theoretical and measured scaling relationships for simple channel networks. (a) Power law scaling between the number of channels and average flux per channel for an ideal flux-preserving binary coalescing network. (b) Scaling relations for the numerical calculations in this paper. (c) Scaling between number of dunite channels and their width for three outcrops in the Ingalls ophiolite, Washington Cascades. Thin lines are fits to individual outcrops, the thick shaded line (with slope $= -3$) is a composite fit.

Appendix A: Derivation and Scaling of Governing Equations

The equations for flow in viscously deformable, permeable media have been discussed in detail by several authors [see *McKenzie*, 1984; *Scott and Stevenson*, 1984, 1986; *Spiegelman*, 1993a, b, c]. The equations for conservation of total mass and momentum of the two-phase system of melt and solid are

$$\frac{\partial \rho_f \phi}{\partial t} + \boldsymbol{\nabla}\cdot\left[\rho_f \phi \mathbf{v}\right] = \Gamma, \tag{A1}$$

$$\frac{\partial \rho_s (1-\phi)}{\partial t} + \boldsymbol{\nabla}\cdot\left[\rho_s (1-\phi) \mathbf{V}\right] = -\Gamma, \tag{A2}$$

$$\phi\left(\mathbf{v}-\mathbf{V}\right) = -\frac{k_\phi}{\mu}\left[\boldsymbol{\nabla} P - \rho_f \mathbf{g}\right], \tag{A3}$$

$$\boldsymbol{\nabla} P = -\boldsymbol{\nabla}\times\eta(\boldsymbol{\nabla}\times\mathbf{V}) + \boldsymbol{\nabla}(\zeta + 4\eta/3)\boldsymbol{\nabla}\cdot\mathbf{V} + \mathbf{G} + \bar{\rho}\mathbf{g}, \tag{A4}$$

$$k_\phi = \frac{a^2 \phi^n}{b}, \tag{A5}$$

where ρ_f and ρ_s are the melt and solid densities, ϕ is the volume fraction of melt (porosity), $\mathbf{v}$ and $\mathbf{V}$ are the melt and solid velocities, and Γ is the total rate of mass transfer from solid to liquid; k_ϕ is the permeability, which is a nonlinear function of porosity (Equation (A5)), μ is the melt viscosity, P is the fluid pressure, and $\mathbf{g}$ is the acceleration due to gravity. Finally, η is the solid shear viscosity, $(\zeta + 4\eta/3)$ is the combination of solid bulk and shear viscosity that controls volumes changes of the matrix, $\mathbf{G}(\eta, \mathbf{V})$ are the cross terms that arise for nonconstant shear viscosity (and vanish if η is constant), and $\bar{\rho} = \rho_f\phi + \rho_s(1-\phi)$ is the mean density of the two phase system. Equations (A1) and (A2) conserve mass for the melt and solid, respectively, and allow mass transfer between the phases. Equation (A3) governs the separation between melt and solid and (A4) governs stress balance and deformation of the solid phase.

To close these equations requires functional forms for the mass transfer rate Γ. For simple adiabatic upwelling, the mass transfer rate can be set to be a function of the upwelling rate [e.g., see *Spiegelman*, 1993c, 1996]. Reactive flows, however, require a more general formulation that, at the minimum, requires tracking the compositions of melt and solid. For an N component system with J simultaneous reactions, we can write $2N$ equations for the conservation of mass of component i in the melt and solid as

$$\frac{\partial \rho_f \phi c_i^f}{\partial t} + \boldsymbol{\nabla}\cdot\left[\rho_f \phi c_i^f \mathbf{v}\right] = \boldsymbol{\nabla}\cdot\rho_f\phi\mathcal{D}_i^f\boldsymbol{\nabla}c_i^f + \sum_{j=1}^{J} c_{ij}^{f*}\Gamma_j \tag{A6}$$

$$\frac{\partial \rho_s (1-\phi) c_i^s}{\partial t} + \boldsymbol{\nabla}\cdot\left[\rho_s (1-\phi) c_i^s \mathbf{V}\right] = -\sum_{j=1}^{J} c_{ij}^{f*}\Gamma_j \tag{A7}$$

where c_i^f and c_i^s are the concentration of component i in the melt and solid, respectively. $\mathcal{D}_i^f$ is the combined diffusivity/dispersivity tensor of component i in the melt (we assume negligible solid diffusion) and c_{ij}^{f*} is the concentration of component i in the fluid that is involved in reaction j. Γ_j is the rate of mass transfer for reaction j. Specific forms for different types of reactions will be introduced below. To make (A6)–(A7) consistent with (A1)–(A2) and the property that the sum of all concentrations in any phase must add to 100% (e.g., $\sum_{i=1}^{N} c_i^f = \sum_{i=1}^{N} c_i^s = \sum_{i=1}^{N} c_{ij}^{f*} = 1$) requires

that the total mass transfer rate be

$$\Gamma = \sum_{j=1}^{J} \Gamma_j \tag{A8}$$

and that $\sum_{i=1}^{N} \boldsymbol{\nabla}\cdot \rho_f \phi \mathcal{D}_i^f \boldsymbol{\nabla} c_i^f = 0$ because only $N-1$ concentrations can freely diffuse. The final component must be antidiffusive to conserve mass. For extensions to more complicated multicomponent systems see *Steefel and Lasaga* [1994].

To make (A1)–(A7) more tractable and amenable to analysis, it is useful to rewrite the equations into potential form and make them dimensionless. *Spiegelman* [1993a] provides a basic recipe for scaling and writing (A1)–(A5) in potential form. To get from (A1)–(A7) to (1)–(4), we follow the analysis of *Spiegelman* [1993a] and *Aharonov et al.* [1995]. To get the dimensional forms of the equations, expand (A2) and define $\mathcal{C} = \boldsymbol{\nabla}\cdot\mathbf{V}$ to yield

$$\frac{\partial \phi}{\partial t} + \mathbf{V}\cdot\boldsymbol{\nabla}\phi = (1-\phi)\mathcal{C} + \frac{\Gamma}{\rho_s}. \tag{A9}$$

Adding (A1) and (A2) and substituting in (A3) and (A4) under the assumptions $\eta = \text{const}$ and neglecting rotational flow yields

$$\begin{aligned} -\boldsymbol{\nabla}\cdot\frac{k_\phi}{\mu}\boldsymbol{\nabla}(\zeta+4\eta/3)\mathcal{C} + \mathcal{C} \\ = -\boldsymbol{\nabla}\cdot\left[\frac{k_\phi \Delta\rho g}{\mu}(1-\phi)\mathbf{k}\right] + \frac{\Delta\rho}{\rho_f\rho_s}\Gamma, \end{aligned} \tag{A10}$$

or substituting $\mathcal{P} = (\zeta+4\eta/3)\mathcal{C}$ yields the equation in terms of excess pressure

$$\begin{aligned} -\boldsymbol{\nabla}\cdot\frac{k_\phi}{\mu}\boldsymbol{\nabla}\mathcal{P} + \frac{\mathcal{P}}{(\zeta+4\eta/3)} \\ = -\boldsymbol{\nabla}\cdot\left[\frac{k_\phi \Delta\rho g}{\mu}(1-\phi)\mathbf{k}\right] + \frac{\Delta\rho}{\rho_f\rho_s}\Gamma. \end{aligned} \tag{A11}$$

By the definitions for $\mathcal{C}$ and $\mathbf{V} = \boldsymbol{\nabla}\mathcal{U}$ we get $\nabla^2\mathcal{U} = \mathcal{C}$.

To get the dimensional equations for conservation of composition, we expand the right-hand side of (A6) and (A7) and substitute in (A1), (A2), and (A8) to get

$$\rho_s(1-\phi)\frac{D_s c_i^s}{Dt} = -\left[\sum_{j=1}^{J}(c_{ij}^{f*} - c_i^s)\Gamma_j\right] \tag{A12}$$

$$\rho_f\phi\frac{D_f c_i^f}{Dt} = \left\{\boldsymbol{\nabla}\cdot\rho_f\phi\mathcal{D}_i^f\boldsymbol{\nabla}c_i^f + \left[\sum_{j=1}^{J}(c_{ij}^{f*} - c_i^f)\Gamma_j\right]\right\}. \tag{A13}$$

To reduce the number of adjustable parameters, it is useful to nondimensionalize (A9)–(A13) with the following natural scaling:

$$\begin{aligned} \phi = \phi_0\phi' \qquad & t = \frac{\delta}{w_0}t', \\ \mathbf{x} = \delta\mathbf{x}' \qquad & \boldsymbol{\nabla} = \frac{1}{\delta}\boldsymbol{\nabla}', \\ (\mathbf{v},\mathbf{V}) = w_0(\mathbf{v},\mathbf{V})' \qquad & \mathcal{U} = \delta w_0\mathcal{U}', \\ \mathcal{C} = \frac{\phi_0 w_0}{\delta}\mathcal{C}' \qquad & \mathcal{P} = \Delta\rho g\mathcal{P}', \\ (\Gamma,\Gamma_j) \;=\; & \frac{\rho_s\phi_0 w_0}{\delta}(\Gamma,\Gamma_j)', \\ (\zeta+4\eta/3) \;=\; & (\zeta+4\eta/3)_0(\zeta+4\eta/3)', \end{aligned}$$

where

$$\delta = \sqrt{\frac{k_0(\zeta+4\eta/3)_0}{\mu}} \tag{A14}$$

$$\phi_0 w_0 = \frac{k_0\Delta\rho g}{\mu} \tag{A15}$$

are the compaction length and the melt separation velocity [e.g., *McKenzie*, 1984; *Spiegelman*, 1993a], where k_0 and $(\zeta+4\eta/3)_0$ are the permeability and solid viscosity at porosity ϕ_0. Substituting these definitions into (A9)–(A13) and dropping primes yields

$$\frac{D_s\phi}{Dt} = (1-\phi_0\phi)\mathcal{C} + \Gamma, \tag{A16}$$

$$-\boldsymbol{\nabla}\cdot k_\phi\boldsymbol{\nabla}\mathcal{P} + \frac{\mathcal{P}}{(\zeta+4\eta/3)} = -\boldsymbol{\nabla}\cdot[k_\phi(1-\phi_0\phi)\mathbf{k}] + \frac{\Delta\rho}{\rho_f}\Gamma, \tag{A17}$$

$$\nabla^2\mathcal{U} = \phi_0\mathcal{C}, \tag{A18}$$

$$\frac{D_s c_i^s}{Dt} = \frac{-\phi_0}{(1-\phi_0\phi)}\left[\sum_{j=1}^{J}(c_{ij}^{f*} - c_i^s)\Gamma_j\right], \tag{A19}$$

$$\frac{D_f c_i^f}{Dt} = \frac{1}{\phi}\left\{\frac{1}{Pe_i}\boldsymbol{\nabla}\cdot\phi\boldsymbol{\nabla}c_i^f + \frac{\rho_s}{\rho_f}\left[\sum_{j=1}^{J}(c_{ij}^{f*} - c_i^f)\Gamma_j\right]\right\}, \tag{A20}$$

where

$$\mathcal{P} = (\zeta+4\eta/3)\mathcal{C}, \tag{A21}$$

$$k_\phi = \phi^n, \tag{A22}$$

$$\mathbf{V} = \boldsymbol{\nabla}\mathcal{U}, \tag{A23}$$

$$\mathbf{v} = \mathbf{V} - \frac{k_\phi}{\phi}\left[\boldsymbol{\nabla}\mathcal{P} - (1-\phi_0\phi)\mathbf{k}\right]. \tag{A24}$$

The three simplifications required to get (1)–(4) are that the reference porosity ϕ_0 is sufficiently small such that (A18) can be neglected (i.e., $\mathbf{V} \approx 0$); that

$$\frac{1}{\rho_f \phi} \boldsymbol{\nabla} \cdot \rho_f \phi \boldsymbol{\nabla} \sim \nabla^2 \tag{A25}$$

and that there is only a single reaction $p_{\rm solid} \rightarrow p_{\rm dissolved}$ and $c_{11}^{f*} = c_R^f = 1$. The rate of this reaction is Γ_R which we assume to be controlled by linear kinetics such that

$$\Gamma_R = RA(\phi, c^s) \left[c_{eq}^f - c^f \right], \tag{A26}$$

where R is a reaction rate per unit area and A is the specific area of the reaction, which depends on the porosity and amount of soluble phase. Equation (A26) states that the reactive dissolution rate is proportional to the difference between the melt composition and the equilibrium composition. If the melt is undersaturated in the reactive component ($c^f < c_{eq}^f$), the solid will dissolve ($\Gamma_R > 0$) otherwise the solid will precipitate. Using the scaling given in (A14), (A26) can be written in dimensionless form as

$$\Gamma_R = DaA'(c_{eq}^f - c^f). \tag{A27}$$

In the more general case of adiabatic background melting and dissolution,

$$\Gamma = \Gamma_0 + \Gamma_R, \tag{A28}$$

where dimensionally

$$\Gamma_0 = \rho_s W \frac{\partial F}{\partial z} \tag{A29}$$

is the mass transfer rate due to adiabatic decompression and is simply proportional to the solid upwelling velocity and the imposed degree of melting F as a function of height. Figure 6 shows details of specific melting runs.

Acknowledgments. This work was supported by NSF grants OCE95-3069 and OCE99-0709. Helpful reviews were provided by C. Steefel and C. Carrigan, and we thank the LDEO BBL for support and inspiration. This is LDEO contribution 6095.

References

Aharonov, E., J. Whitehead, P. B. Kelemen, and M. Spiegelman, Channeling instability of upwelling melt in the mantle, *J. Geophys. Res.*, *100*, 20,433–20,450, 1995.

Aharonov, E., M. Spiegelman, and P. B. Kelemen, Three-dimensional flow and reaction in porous media: Implications for the Earth's mantle and sedimentary basins, *J. Geophys. Res.*, *102*, 14,821–14,834, 1997.

Barnouin-Jha, K., E. M. Parmentier, and D. W. Sparks, Buoyant mantle upwelling and crustal production at oceanic spreading centers: On-axis segmentation and off-axis melting, *J. Geophys. Res.*, *102*, 11,979–11,989, 1997.

Boudier, F., and R. G. Coleman, Cross section through the peridotite in the Samail Ophiolite, southeastern Oman Mountains, *J. Geophys. Res.*, *86*, 2573–2592, 1981.

Brearley, M., C. Scarfe, and H. Brenner, Dissolution rates of upper mantle minerals in an alkali basalt melt at high pressure: An experimental study and implications for ultramafic xenolith survival, *J. Petrol.*, *27*, 1157–1182, 1986.

Ceuleneer, G., M. Monnereau, and I. Amri, Thermal structure of a fossil mantle diapir inferred from the distribution of mafic cumulates, *Nature*, *379*, 149–153, 1996.

Chadam, J., D. Hoff, E. Merino, P. Ortoleva, and A. Sen, Reactive infiltration instability, *J. Appl. Math.*, *36*, 207–221, 1986.

Connolly, J. A., and Y. Y. Podladchikov, Compaction-driven fluid flow in viscoelastic rock, *Geodin. Acta*, *11*, 55–84, 1998.

Daccord, G., Dissolutions, evaporations, etchings, in *The fractal approach to heterogeneous chemistry*, edited by D. Avnir, pp. 183–197, John Wiley and Sons, New York, 1989.

Daines, M. J., and D. L. Kohlstedt, Influence of deformation on melt topology in peridotites, *J. Geophys. Res.*, *102*, 10,257–10,271, 1997.

Dick, H. J. B., and J. H. Natland, Late-stage melt evolution and transport in the shallow mantle beneath the East Pacific Rise, *Proc. Ocean Drill. Program Sci. Results*, *147*, 103–134, 1996.

Dick, H. J. B., and J. M. Sinton, Compositional layering in alpine peridotites: Evidence for pressure solution creep in the mantle, *J. Geol.*, *87*, 403–416, 1979.

Forsyth, D. W., et al., Imaging the deep seismic structure beneath a mid-ocean ridge: The MELT experiment, *Science*, *280*, 1215–1217, 1998.

Hall, C., and E. M. Parmentier, Effects of melt-dependent viscosity and mantle heterogeneities on melt migration, *Trans. AGU*, *79*(45), F990, 1998, Fall Meet. Suppl.

Hart, S. R., Equilibration during mantle melting: A fractal tree model, *Proc. Natl. Acad. Sci. U.S.A.*, *90*, 11,914–11,918, 1993.

Hirschmann, M., Melt pathways in the mantle, *Nature*, *375*, 737–738, 1995.

Hirth, G., and D. L. Kohlstedt, Water in the oceanic upper mantle: Implications for rheology, melt extraction and the evolution of the lithosphere, *Earth Planet. Sci. Lett.*, *144*, 93–108, 1996.

Hoefner, M., and H. Fogler, Pore evolution and channel formation during flow and reaction in porous media, *AIChE J.*, *34*, 45–54, 1988.

Johnson, K. T. M., and H. J. B. Dick, Open system melting and temporal and spatial variation of peridotite and basalt at the Atlantis II fracture zone, *J. Geophys. Res.*, *97*, 9219–9241, 1992.

Johnson, K. T. M., H. J. B. Dick, and N. Shimizu, Melting in the oceanic upper mantle: An ion microprobe study of diopsides in abyssal peridotites, *J. Geophys. Res.*, *95*, 2661–2678, 1990.

Jull, M., and D. McKenzie, The effect of deglaciation on mantle melting beneath iceland, *J. Geophys. Res.*, *101*, 21,815–21,828, 1996.

Kelemen, P. B., and H. J. B. Dick, Focused melt flow and localized deformation in the upper mantle: Juxtaposition of replicative dunite and ductile shear zones in the Josephine peridotite, SW Oregon, *J. Geophys. Res.*, *100*, 423–438, 1995.

Kelemen, P. B., H. J. Dick, and J. E. Quick, Formation of harzburgite by pervasive melt rock reaction in the upper mantle, *Nature*, *358*, 635–641, 1992.

Kelemen, P. B., N. Shimizu, and V. J. M. Salters, Extraction of mid-ocean-ridge basalt from the upwelling mantle by focused flow of melt in dunite channels, *Nature*, *375*, 747–753, 1995a.

Kelemen, P. B., J. A. Whitehead, E. Aharonov, and K. A. Jordahl, Experiments on flow focusing in soluble porous media, with applications to melt extraction from the mantle., *J. Geophys. Res.*, *100*, 475, 1995b.

Kelemen, P. B., G. Hirth, N. Shimizu, M. Spiegelman, and H. J. B. Dick, A review of melt migration processes in the adiabatically upwelling mantle beneath oceanic spreading ridges, *Philos. Trans. R. Soc. London, Ser. A*, *355*, 283–318, 1997.

Kelemen, P. B., M. Braun, and G. Hirth, Spatial distribution of melt conduits in the mantle beneath oceanic spreading ridges: Observations from the Ingalls and Oman ophiolites, *Geochem. Geophys. Geosyst.*, *1*, paper 1999GC000012, 2000.

Klein, E. M., and C. H. Langmuir, Global correlations of ocean ridge basalt chemistry with axial depth and crustal thickness, *J. Geophys. Res.*, *92*, 8089–8115, 1987.

Kuo, L. C., and R. J. Kirkpatrick, Kinetics of crystal dissolution in the system diopside-forsterite-silica, *Am. J. Sci.*, *285*, 51–90, 1985a.

Kuo, L. C., and R. J. Kirkpatrick, Dissolution of mafic minerals and its implications for the ascent velocities of peridotite-bearing basaltic magmas, *J. Geol.*, *93*, 691–700, 1985b.

Lundstrom, C. C., J. B. Gill, Q. Williams, and M. R. Perfit, Mantle melting and basalt extraction by equilibrium porous flow, *Science*, *270*, 1958–1961, 1995.

McKenzie, D., The generation and compaction of partially molten rock, *J. Petrol.*, *25*, 713–765, 1984.

Nicolas, A., *Structures of Ophiolites and Dynamics of Oceanic Lithosphere*, vol. 4 of *Petrology and Structural Geology*, Kleuwer Acad., Norwell, Mass., 1989.

Nicolas, A., Melt extraction from mantle peridotites: Hydrofracturing and porous flow, with consequences for oceanic ridge activity, in *Magma Transport and Storage*, edited by M. P. Ryan, pp. 159–174, John Wiley and Sons, New York, 1990.

O'Hara, M. J., Primary magmas and the origin of basalts, *Scot. J. Geol.*, *1*, 19–40, 1965.

Ortoleva, P., E. Merino, C. Moore, and J. Chadam, Geochemical self-organization, I, reaction-transport feedbacks, *Am. J. Sci.*, *287*, 979–1007, 1987.

Phipps Morgan, J., Melt migration beneath mid-ocean spreading centers, *Geophys. Res. Lett.*, *14*, 1238–1241, 1987.

Press, W. H., B. P. Flannery, S. A. Teukolsky, and W. T. Vetterling, *Numerical Recipes*, 2nd ed., Cambridge Univ. Press, New York, 1992.

Quick, J. E., The origin and significance of large, tabular dunite bodies in the Trinity Peridotite, northern California, *Contrib. Mineral. Petrol.*, *78*, 413–422, 1981.

Ribe, N., The deformation and compaction of partially molten zones, *Geophys. J. R. Astron. Soc.*, *83*, 137–152, 1985.

Richardson, C. N., Melt flow in a variable viscosity matrix, *Geophys. Res. Lett.*, *25*, 1099–1102, 1998.

Ross, D. K., and D. Elthon, Extreme incompatible trace-element depletion of diopside in residual mantle from south of the Kane Fracture Zone, *Proc. Ocean Drill. Program, Sci. Results*, *153*, 277–284, 1995.

Salters, V. J. M., and S. R. Hart, The hafnium paradox and the role of garnet in the source of mid-ocean ridge basalts, *Nature*, *342*, 420–422, 1989.

Scott, D. R., and D. Stevenson, Magma solitons, *Geophys. Res. Lett.*, *11*, 1161–1164, 1984.

Scott, D. R., and D. Stevenson, Magma ascent by porous flow, *J. Geophys. Res.*, *91*, 9283–9296, 1986.

Sims, K. W. W., D. J. Depaolo, M. T. Murrell, W. S. Baldridge, S. J. Goldstein, and D. A. Clague, Mechanisms of magma generation beneath Hawaii and mid-ocean ridges: Uranium/thorium and samarium/neodymium isotopic evidence, *Science*, *267*, 508–512, 1995.

Slater, L., M. Jull, D. McKenzie, and K. Gronvold, Deglaciation effects on mantle melting under Iceland: Results from the northern volcanic zone, *Earth Planet. Sci. Lett.*, *164*, 151–164, 1998.

Sleep, N., Tapping of melt by veins and dikes, *J. Geophys. Res.*, *93*, 10,255–10,272, 1988.

Sparks, D. W., and E. M. Parmentier, Melt extraction from the mantle beneath spreading centers, *Earth Planet. Sci. Lett.*, *105*, 368–377, 1991.

Spiegelman, M., Flow in deformable porous media. part 1. Simple analysis, *J. Fluid Mech.*, *247*, 17–38, 1993a.

Spiegelman, M., Flow in deformable porous media. part 2. Numerical analysis—The relationship between shock waves and solitary waves, *J. Fluid Mech.*, *247*, 39–63, 1993b.

Spiegelman, M., Physics of melt extraction: Theory, implications and applications, *Philos. Trans. R. Soc. London, Ser. A*, *342*, 23–41, 1993c.

Spiegelman, M., Geochemical consequences of melt transport in 2-D: The sensitivity of trace elements to mantle dynamics, *Earth Planet. Sci. Lett.*, *139*, 115–132, 1996.

Spiegelman, M., and P. Kenyon, The requirements for chemical disequilibrium during magma migration, *Earth Planet. Sci. Lett.*, *109*, 611–620, 1992.

Spiegelman, M., and D. McKenzie, Simple 2-D models for melt extraction at mid-ocean ridges and island arcs, *Earth Planet. Sci. Lett.*, *83*, 137–152, 1987.

Staniforth, A., and J. Cote, Semi-Lagrangian integration schemes for atmospheric models—A review, *Mont. Weather Rev.*, *119*, 2206–2223, 1991.

Steefel, C., and A. Lasaga, Evolution of dissolution patterns, in *Chemical Modeling in Aqueous Systems II*, edited by D. Melchior and R. Bassett, pp. 212–225, Am. Chem. Soc., Washington, D.C., 1990.

Steefel, C. I., and A. C. Lasaga, A coupled model for transport of multiple chemical species and kinetic precipitation/dissolution reactions, *Am. J. Sci.*, *294*, 529–592, 1994.

Stevenson, D. J., Spontaneous small-scale melt segregation in partial melts undergoing deformation, *Geophys. Res. Lett.*, *16*, 1067–1070, 1989.

Stolper, E. A., A phase diagram for mid-ocean ridge basalts: Preliminary results and implications for petrogenesis, *Contrib. Mineral. Petrol.*, *74*, 13–27, 1980.

Suhr, G., Melt migration under oceanic ridges: Inferences from reactive transport modelling of upper mantle hosted dunites, *J. Petrol.*, *40*, 575–599, 1999.

Takahashi, N., Evidence for melt segregation towards fractures in the Horoman mantle peridotite complex, *Nature*, *359*, 52–55, 1992.

Varfalvy, V., R. Hebert, and J. H. Bedard, Interactions between melt and upper-mantle peridotites in the North Arm Mountain massif, Bay of Islands ophiolite, Newfoundland, Canada: Implications for the genesis of boninitic and related magmas, *Chem. Geol.*, *129*, 71–90, 1996.

Vera, E. E., J. C. Mutter, P. Buhl, J. A. Orcutt, A. J. Harding, M. E. Kappus, R. S. Detrick, and T. M. Brocher, The structure of 0- to 0.2-m.y.-old oceanic crust at 9°N on the East Pacific Rise from expanded spread profiles, *J. Geophys. Res.*, *95*, 15,529–15,556, 1990.

Zhang, Y., D. Walker, and C. Lesher, Diffusive crystal dissolution, *Contrib. Mineral. Petrol.*, *102*, 492–513, 1989.

Zimmerman, M. E., S. Q. Zhang, D. L. Kohlstedt, and S. Karato, Melt distribution in mantle rocks deformed in shear, *Geophys. Res. Lett.*, *26*, 1505–1508, 1999.

M. Spiegelman, Lamont-Doherty Earth Observatory of Columbia University, Palisades, NY 10964. (einat@ldeo.columbia.edu; mspieg@ldeo.columbia.edu)

P. Kelemen, Woods Hole Oceanographic Institute, Woods Hole, MA 02543 (peterk@whoi.edu)

E. Aharonov, Environmental Sciences and Energy Research Department, Weizmann Institute of Science, 109 Sussman Bldg, Rehovot, 76100, Israel (einat.aharonov@weizmann.ac.il)

Received August 9, 1999; revised June 5, 2000; accepted June 28, 2000.

This preprint was prepared with AGU's LaTeX macros v5.01, with the extension package 'AGU^{++}' by P. W. Daly, version 1.6b from 1999/08/19.